Journal of Materials Research and Technology 27 (2023) 3151–3160

Contents lists available at ScienceDirect

Journal of Materials Research and Technology

journal homepage: www.elsevier.com/locate/jmrt

Anisotropy in 3D-printed $(FeCoNi)_{86}Al_7Ti_7$ high entropy alloy

Li-Xue Liu [a], Jie Pan [a,**], Peng-Cheng Zhang [a], Cheng Zhang [a], Jing-Yu Xu [a], Rong Guo [a], Zi-Bin Chen [b,c], K.C. Chan [b,c], Lin Liu [a,*]

[a] State Key Laboratory of Material Processing and Die & Mould Technology and School of Materials Science and Engineering, Huazhong University of Science and Technology, 430074 Wuhan, China

[b] State Key Laboratory of Ultra-precision Machining Technology, Department of Industrial and Systems Engineering, The Hong Kong Polytechnic University, Hung Hom, Kowloon 999077, Hong Kong, China

[c] Research Institute for Advanced Manufacturing, Department of Industrial and Systems Engineering, The Hong Kong Polytechnic University, Hung Hom, Kowloon 999077, Hong Kong, China

ARTICLE INFO

Keywords:
High entropy alloy
Selective laser melting
Mechanical properties
Anisotropy
Crack propagation

ABSTRACT

Anisotropic microstructure and mechanical properties are vital considerations in the practical applications of 3D-printed metallic materials; however, limited attention has been given to the anisotropy in 3D-printed high entropy alloys (HEAs). This study systematically explores the structural and mechanical anisotropy of $(FeCoNi)_{86}Al_7Ti_7$ HEA with low porosity, fabricated via selective laser melting (SLM). The SLM process, characterized by directional and repeated thermal dissipation, creates an anisotropic structure consisting of epitaxial columnar grains aligned parallel to the building direction, subsequently influencing mechanical anisotropy. Tensile testing unveils slight anisotropy in strength but significant differences in ductility for the SLMed HEA. The 0° sample demonstrates the optimal combination of strength and plasticity, boasting a tensile elongation of 31.5 %, approximately 2.6 times higher than that of the 45° and 90° samples. The post-mortem microscopic analysis indicates that this ductility anisotropy primarily originates from the crack propagation behavior. In the 0° sample, crack propagation occurs through both intergranular and transgranular modes, with the robust interactions between the two modes providing an obstruction to crack propagation. On the contrary, crack widening occurs essentially along the continuous melting pool boundaries (MPBs) in 45° and 90° samples, leading to the straight crack propagation path along the MPBs and therefore reduced ductility.

1. Introduction

High entropy alloys (HEAs) are a new class of metallic materials with multiple principal primary elements in equal or nearly equimolar amounts [1,2], have gained significant attention due to their exceptional mechanical properties [3–5]. The high mixing configurational entropies of HEAs contribute to the stabilization of single solid solutions with simple crystal structures [6–8], resulting in high viscosity and low fluidity of HEA metls [9,10]. As a result, it is challenging to cast large-sized and complex-shaped HEA components, except for a few eutectic HEAs [11,12]. Moreover, costly post-process techniques including cold rolling and thermal treatments are essential to eliminate casting flaws [13]. Therefore, there is of vital necessity to develop effective and efficient techniques to fabricate this new class of alloys, among which three-dimensional (3D) printing stands out. Nowadays, 3D printing has become an alternative method for manufacturing complicated HEA components [14,15].

Selective laser melting (SLM), a widely used 3D-printing technique, offers substantial benefits over traditional casting for near-net shaping of large-scale and complex-geometry components [16]. Furthermore, the rapid solidification process during SLM promotes the refined microstructures, leading to improved mechanical properties of 3D-printed components [17]. To date, many HEA systems, for example, CoCrFeNi [18], CoCrFeMnNi [17], AlCoCrFeNi [19], as well as $AlCoCrFeNi_{2.1}$ [20] have been developed, and they exhibit a favorable combination of strength and ductility under tesile deformation. For instance, Kim et al. developed a high-performance CoCrFeMnNi HEA by the interstitial oxygen addition, which exhibited superior tensile strengths of 0.92 GPa and 1.45 GPa at 298 K and 77 K, respectively, much higher than most reported CoCrFeMnNi HEAs, while maintaining a high tensile strain

* Corresponding author.
** Corresponding author.
E-mail addresses: jpan@hust.edu.cn (J. Pan), lliu2000@mail.hust.edu.cn (L. Liu).

https://doi.org/10.1016/j.jmrt.2023.10.161
Received 24 August 2023; Accepted 16 October 2023
Available online 19 October 2023

over 20 % [21]. However, the SLM-manufactured alloys usually undergo a complex cyclic thermal history and layered directional heat extraction, which bring about complex microstructure [22,23], such as printing defects, texture, epitaxial columnar grains, and melting pool boundaries (MPBs), resulting in the anisotropic properties [24].

Given that the microstructure governs the materials' performances, especially for load-bearing structural components, it is crucial to understand the orientation-dependent properties in additive manufactured materials [25,26]. Paul et al. found that the strength of SLMed AlSi10Mg with minimal anisotropy is controlled by grain size and cellular structure; however, the arrangement of MPBs leads to anisotropy in ductility and fracture toughness when loaded in different directions [27]. Kuo et al. identified that interdendritic δ-phase precipitates are responsible for the mechanical anisotropy of 3D-printed IN718, which provide the initial site and path of cracks during the tensile test, leading to the worse ductility in the horizontal-direction specimen [28]. In addition, 3D-printing defects, such as pores and lack of fusion layers, can also affect the directional properties of materials. For example, Jeon et al. believed the pores have a dominant effect on mechanical anisotropy [29]. Their findings showed that 316L stainless steel processed by SLM exhibited a much lower elongation in the building direction (BD) because large stress concentration would be generated around the pores, which is much more severe at the sharp tip of the pore perpendicular to the loading direction.

Numerous studies have investigated the process parameters, microstructure, mechanical properties, and processability of various HEA systems [30,31]. However, the anisotropy in microstructure and mechanical properties of 3D-printed HEAs has received less attention. Zhang et al. conducted an investigation into the hierarchical microstructure and mechanical properties of the laser powder bed fusion (LPBF)-built CoCrFeMnNi HEA. They examined properties along the horizontal, diagonal, and vertical directions and discovered that both columnar grain morphology and texture influence tensile anisotropy in terms of strength and elongation [32]. Additionally, Zhang et al. compared the microstructures and anisotropy of tensile properties of $Fe_{49.5}Mn_{30}Co_{10}Cr_{10}C_{0.5}$ HEA printed by LPBF with stripe and chessboard scanning strategies. Both stripe and chessboard samples exhibited columnar and equiaxial grains with a preferred <1 1 0> orientation parallel to BD. However, chessboard samples demonstrated minimal tensile anisotropy compared to stripe samples when loaded along different planes. This observation is attributed to the interplay between preferential grain growth mechanisms and the direction of the temperature gradient during the LPBF process [33]. Recently, $(FeCoNi)_{86}Al_7Ti_7$ HEA has gained increasing research interest due to its outstanding mechanical properties [34] and excellent printability [35], making it a promising structural material for practical applications. The SLM process tends to induce pronounced anisotropy in microstructure and mechanical properties [23,32], affecting its service performance since most service loading conditions are anisotropic and directional. In this work, we explore the microstructural features and mechanical properties of SLMed $(FeCoNi)_{86}Al_7Ti_7$ HEA in different orientations and discuss the origins of microstructural and mechanical anisotropy.

2. Experimental procedure

2.1. Samples preparation

Gas atomized powders with a nonimal composition of $(FeCoNi)_{86}Al_7Ti_7$ (at%) were used as the feedstock. SLM experiments were operated on a commercial machine (FORWEDO LM-120, Forwedo) equipped with a Nd: YAG fiber laser device. The fiber laser has a maximum output power of 500 W, a wavelength of 1.06 μm, and an 80 μm spot diameter. The powder used for 3D printing has an average equivalent diameter of approximately 41 μm. The chemical composition of the pre-alloyed powder is shown in Table S1. To ensure the oxygen concentration remained below 100 ppm during the printing proces, the chamber was vacuumed and then protected by argon atmosphere. Fig. 1a shows the schematic of the scanning strategy, where the laser scanning was rotated 67° between adjacent layers (N^{th} and $(N+1)^{th}$) to minimize the thermal stress of the printed sample on the building plane (X and Y directions). The detailed parameters used in the present SLM process are as follows: the laser power of 260 W, scanning speed of 800 mm s^{-1}, a layer thickness of 50 μm, and hatching space of 60 μm. To investigate the mechanical anisotropy of SLMed samples, three group samples with various orientations (i.e., 0°, 45°, and 90°) are extracted from the SLM-processed blocks for tensile testing, as illustrated in Fig. 1b.

2.2. Microstructure characterization

The relative density measurement of the 3D-printed $(FeCoNi)_{86}Al_7Ti_7$ HEAs was based on the Archimedes principle. Phase analysis and dislocation density evaluation of SLMed samples were characterized by X-ray diffraction (XRD, 7000SX, Shimadzu) with Cu Kα radiation at 40 kV and 30 mA. The scanning rate was set to be 1.5°/min, covering a range of 20°–100°. The Williamson-Hall method [36,37] was utilized for dislocation density estimation, with the full width at half maximum of the annealed LaB_6 powder serving as the instrumental broadening. Extensive microstructure investigation was conducted using optical microscopy (OM), scanning electron microscopy (SEM, FEI Sirion 200 and Gemini SEM 300), electron back-scattered diffraction (EBSD, Aztec Nordlys Max3) analysis, and transmission electron microscopy (TEM, FEI Tecnai G2 F30, 300 kV). For the EBSD tests, the step size is 1.0 μm and the voltage is 20 kV. For TEM characterization, the samples were mechanically polished to foils with a thickness of around 30 μm, and then the foils were further thinned by the precision ion polishing machine (Gatan PIPS II 695).

2.3. Mechanical testing

The tensile behavior of 3D-printed HEAs was investigated at room temperature by a Zwick machine (Zwick/Roell 020) with a strain rate of 10^{-3} s^{-1}. Tensile specimens were machined into dog-bone-shape using wire-cutting, with a cross-section of 2.5 mm × 1.5 mm and a gauge length of 12 mm. All surfaces of the tensile samples were polished to achieve a surface roughness $R_a \leq 0.8$. The chamfer between the chuck and the gauge length was placed on the fixture, enabling the Zwick machine's sensor to measure gauge length displacement, ensuring precise strain control. For experiment repeatability and reliability, the tensile tests of samples in three orientations (marked as 0°, 45°, and 90° samples) were conducted and repeated at least three times, respectively. To reveal the microstructure evolution during plastic deformation, the microstructures before and after tensile deformation were examined by SEM and TEM.

2.4. Finite element modeling (FEM) simulation of thermal field

The grain morphology of metals during the SLM process depends on local solidification conditions, including the thermal gradient (G) and the solidification rate (R) at the liquid-solid interface of the melting pool (MP). To evaluate the solidification mechanism of columnar grains, a thermal analysis model was established by ABAQUS software (ABAQUS 6.10, Dassault, France). The ABAQUS subroutine DFLUX was utilized to apply a Gaussian distributed moving heat flux. The sample dimensions are 1 mm × 1 mm × 0.5 mm, and the mesh size in X, Y, and Z axis is set at 0.01 mm × 0.01 mm × 0.01 mm. The G and R values can be obtained by the following equations.

$$R\ (\mathrm{m/s}) = \frac{\text{Cooling Rate (K/s)}}{\text{Thermal Gradient (K/m)}} \quad (1)$$

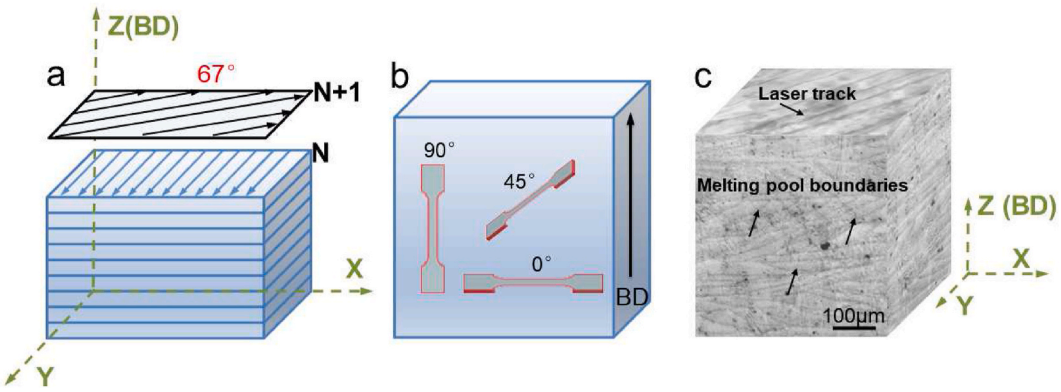

Fig. 1. (a) A schematic of the scanning strategy used in the present SLM process. (b) A schematic showing the geometry of the as-built samples in three different build orientation. (c) 3D OM morphology of the as-SLMed $(FeCoNi)_{86}Al_7Ti_7$ samples.

$$\text{Cooling Rate (K / s)} = \frac{dT}{dt} \tag{2}$$

The parameters required for FEM analysis, such as thermal conductivity, specific heat capacity, thermo-physical properties and processing parameters, are provided in Tables S2 and S3 in the Supplementary Materials.

3. Results

3.1. Microstructural anisotropy in the SLMed $(FeCoNi)_{86}Al_7Ti_7$ HEA

Fig. 1c displays the 3D OM image of the SLMed $(FeCoNi)_{86}Al_7Ti_7$ sample, which allows the visualization of MPBs and the scan tracks. The MPs, which have a half-cylindrical shape, are generally perpendicular to BD. Observing the MPs from multiple directions reveals varied morphologies: a semi-elliptical shape from the Y direction, a strike-like shape from Z direction, and a combination morphology of semi-elliptical shape and stripe-like shape from the 45° direction (i.e., 45° sample), as shown in Fig. S1.

Fig. 2 presents the SEM and EBSD images of the SLMed HEA sample

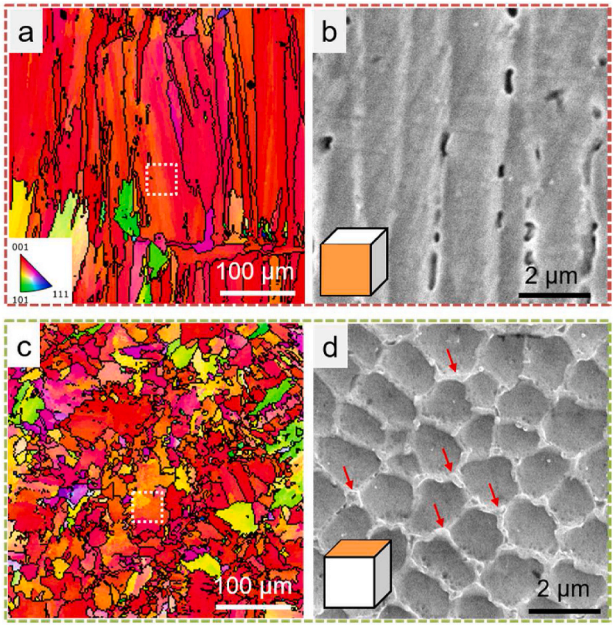

Fig. 2. EBSD IPF and SEM morphology of SLMed HEAs from the (a, b) side view and (c, d) top view, where the black lines in IPF maps are corresponding to high angle grain boundaries (HAGBs).

along and perpendicular to the BD, revealing an anisotropic structure consisting of columnar grains parallel to the BD. From the side view shown in Fig. 2a, columnar grains with a width of ~20 μm and length of ~200 μm grown across the MPs along the BD are observed. These columnar grains exhibit an extremely high length/width ratio (>10) and severe crystallographic texture along the <0 0 1> direction (preferred solidification orientation in face-centered cubic (FCC) metals) [27,38], divided by high angle grain boundaries (HAGBs). From the top view perpendicular to the BD (Fig. 2c), the equiaxial grains with an average size of ~10 μm are observed [39]. A close observation by SEM from side and top views shows that the 1–2 μm sized cellular sub-structure inside each large columnar grain, as shown in Fig. 2b and d. The cell boundaries are decorated with nanoprecipitates, as indicated by the red arrows, which are a result of the directional and repeated thermal dissipation during the SLM process [40].

Further detailed sub-grain microstructure analysis of the SLMed $(FeCoNi)_{86}Al_7Ti_7$ samples was conducted using TEM, perpendicular and parallel to the BD, respectively. From the top view, it is clear that the sub-grain cells have the size of 1–2 μm and their boundaries have a thickness of ~100 nm (Fig. 3a), which agrees with the SEM observations in Fig. 2. The corresponding selected area electron diffraction (SAED) pattern of the SLMed HEA reveals an FCC structure with $L1_2$ superlattice spots, suggesting that the short-range orderings (SROs) exsit in HEAs [41,42]. The same sub-structure with a columnar shape is observed from the side view, as shown in Fig. 3b. A mass of entwined string-like dislocations is distributed on the cellular and columnar structure walls, with certain entangled dislocation networks implanted in specific cells/columns of several hundred nanometers. Additionally, nanoprecipitates (~200 nm) can be found on the cellular boundaries (as depicted in Fig. 3a and b), identified as $L2_1$ phase according to the SAED patterns. From the EDS elemental analysis (Fig. 3c), it is evident that the $L2_1$ nanoprecipitates are enriched in Al and Ti elements and depleted in Fe, Co, and Ni elements. The constituent elements is homogeneous within the cell sub-structure (see the bright region of HADDF image in Fig. 3c), while the cell boundaries are enriched Ti element and depleted in Fe element obviously. The chemical composition of the SLMed $(FeCoNi)_{86}Al_7Ti_7$ HEA is shown in Table 1. The formation of the unique cellular sub-structure is induced by rapid solidification and constitutional supercooling in the SLM process.

3.2. Mechanical anisotropy in the SLMed $(FeCoNi)_{86}Al_7Ti_7$ HEA

To explore the BD-related mechanical anisotropy in SLMed $(FeCoNi)_{86}Al_7Ti_7$ HEA, the tensile behavior of samples with three orientations (marked as 0°, 45°, and 90° samples, see Fig. 1b) was evaluated, and the representative engineering stress-strain curves are shown in Fig. 4a. Overall, all SLMed $(FeCoNi)_{86}Al_7Ti_7$ samples display outstanding mechanical performance with high fracture strength (>1000 MPa) and

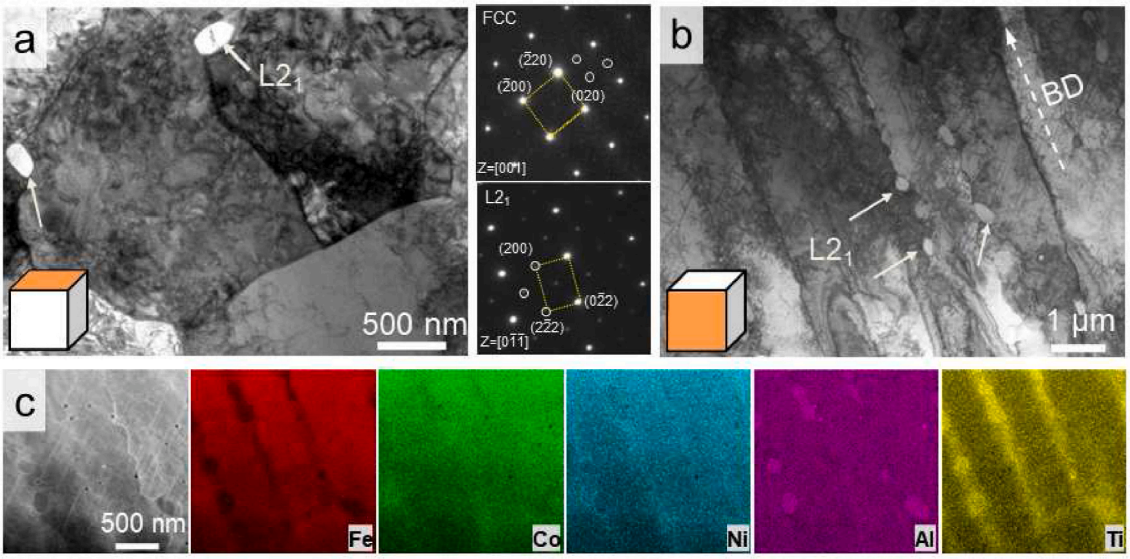

Fig. 3. Bright-field TEM images from the (a) top view and (b) side view showing the cellular and columnar structure of SLMed $(FeCoNi)_{86}Al_7Ti_7$ HEA, with the inset of the SAED patterns of FCC matrix and $L2_1$ nanoprecipitates. (c) STEM image and the corresponding elements distribution of side view.

Table 1
Chemical composition of the SLMed $(FeCoNi)_{86}Al_7Ti_7$ HEA.

	Fe	Co	Ni	Al	Ti
Nominal	28.67	28.67	28.67	7.00	7.00
Matrix	32.46	27.36	26.50	6.93	6.74
$L2_1$	18.94	25.17	26.52	11.41	17.96

large elongation (>10 %), exceeding most reported 3D-printed HEAs [10]. However, apparent mechanical anisotropy still exists in the present SLMed HEA, similar to the cold-rolled HEAs [43]. The 45° sample has the highest yield strength of 752 MPa, which is 4 % and 8 % higher than that in 0° and 90° samples, respectively. However, these samples have a similar ultimate strength of ~1050 MPa. Compared to the strength, the tensile elongation of the three samples varies more significantly. 0° sample has a tensile elongation of 31.5 %, which is ~2.6 times higher than that of 45° and 90° samples (i.e., 13.2 % and 11.2 %, respectively). Meanwhile, 0° sample also has a steady strain hardening capacity compared to 45° and 90° samples, leading to more uniform deformation (Fig. S2).

To offer an intuitive comparison, the measured yield strength (σ_y), tensile strength (σ_{UTS}), and tensile elongation (ε_{EL}) are summarized in Fig. 4b and Table 2, from which the mechanical anisotropy in the SLMed $(FeCoNi)_{86}Al_7Ti_7$ HEA is more evident. 45° sample shows the highest yield strength, while 0° sample has the highest elongation and the best combination of strength and plasticity. This mechanical anisotropy should be related to the anisotropic structure formed during the SLMed process [24,44], which will be discussed later.

Fig. 5 shows the side and fracture morphologies of the SLMed samples with three orientations after tensile testing. 0° and 45° samples show a shear fracture behavior with obvious necking (Fig. 5a and d), which is in contrast to the extension fracture and no obvious necking in the 90° sample (Fig. 5g). All samples exhibit a fracture morphology with micro-scale dimple (Fig. 5c, f, and i), indicating a characteristic of

Table 2
Average grain size (d) and Taylor factor (M), yield strength (σ_y), ultimate strength (σ_{UTS}), and tensile elongation (ε_{EL}) of the SLMed $(FeCoNi)_{86}Al_7Ti_7$ HEA samples with the orientation of 0°, 45°, and 90°.

Samples	d (μm)	M	σ_y (MPa)	σ_{UTS} (MPa)	ε_{EL} (%)
0°	12.6	3.12 ± 0.39	723 ± 1	1099 ± 3	31.5 ± 0.5
45°	13.0	3.20 ± 0.35	752 ± 4	1065 ± 2	13.2 ± 1.5
90°	17.1	2.93 ± 0.32	696 ± 3	1038 ± 4	11.2 ± 1.5

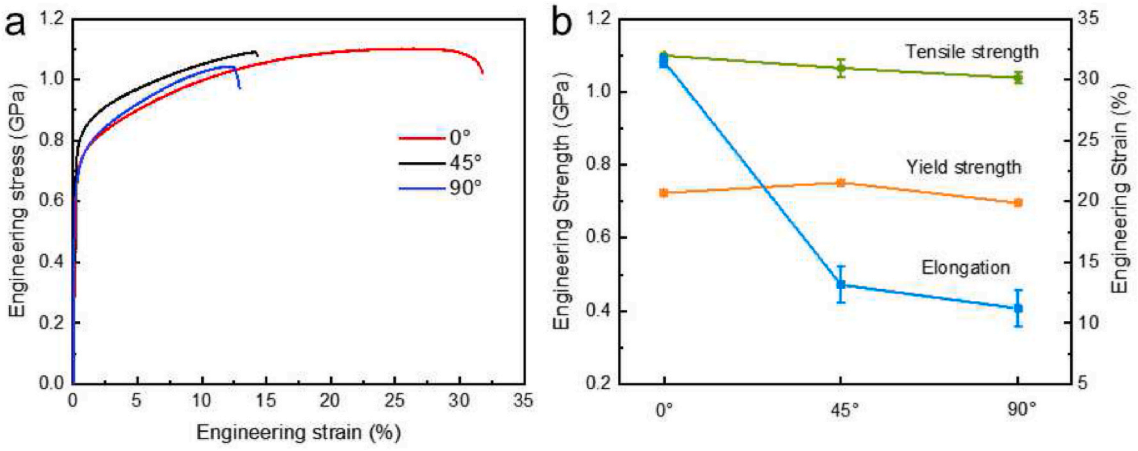

Fig. 4. (a) Engineering stress-strain curves and (b) the yield strength, ultimate strength and elongation of the SLMed samples with various orientations.

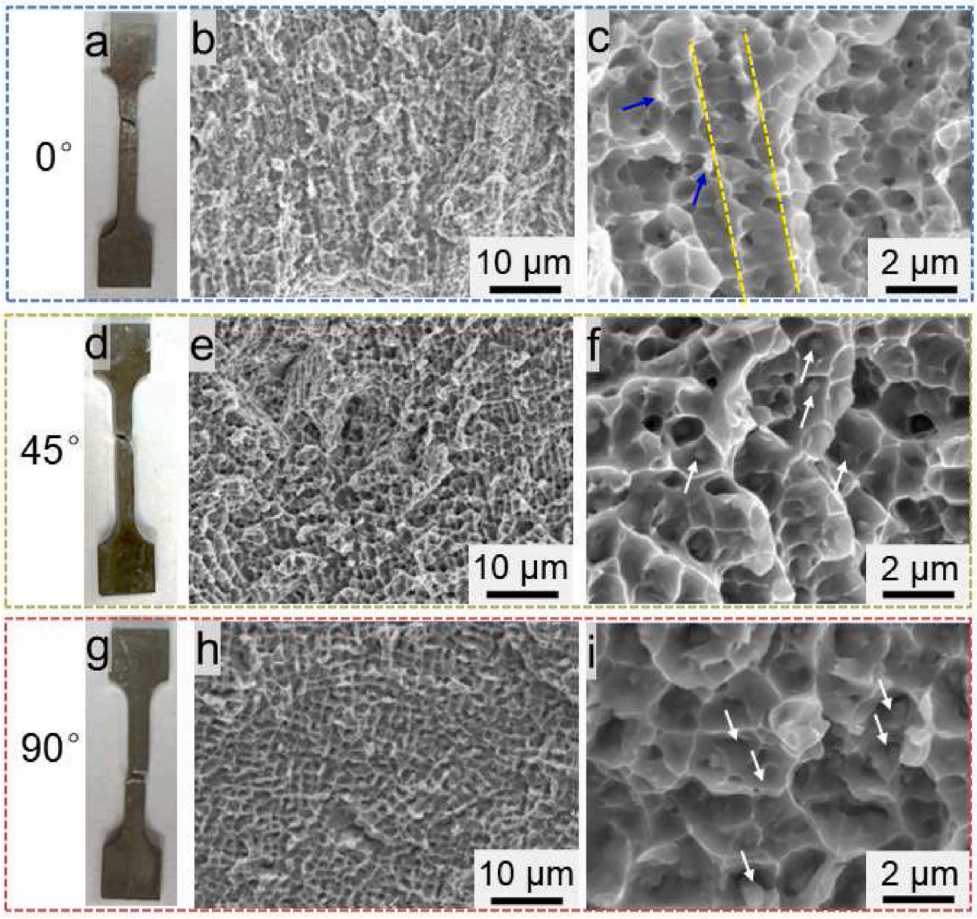

Fig. 5. Side and fracture morphologies of (a–c) 0°, (d–f) 45°, (g–i) 90° samples after tensile testing.

ductile fracture [45]. The dimple size is ~1 μm, which is comparable to the cellular structure dimension. However, three samples have distinct dimple characteristics. The dimple morphology on the fracture surface of the 0° sample is directional, roughly along the BD (Fig. 5b and c), suggesting that the crack propagation process occurs along the columnar grains. More importantly, no nanoparticles are detected inside the dimples, suggesting the homogenous nucleation of the voids. In contrast, the dimples are random in the 45° and 90° samples, and nanoparticles with a size of ~200 nm are distributed inside most dimples, as indicated by the white arrows in Fig. 5f and i. In light of the size, these nanoparticles should correspond to the $L2_1$ precipitates, as presented in Figs. 2 and 3. As FCC matrix and $L2_1$ precipitations have distinct chemical compositions and crystal structures, their strength/hardness would vary significantly. The mechanical incompatibility between the FCC matrix and $L2_1$ particles results in the debonding at the cell interface, leading to the preferential nucleation and subsequent coalescence of the micro-voids. These observations imply that the different fracture mechanisms contribute to the anisotropic mechanical properties in three loading directions.

It should be noted that all SLMed samples exhibit no apparent pore-defects on the fracture surface, which is different from the porosity in many previously reported HEAs prepared by SLM [29,46], where process-induced pores serve as stress raisers and eventually lead to crack initiation and failure. This observation confirms the near-full density of the present SLMed HEA, i.e., 99.43 %. In other words, the limited pores in the present SLMed $(FeCoNi)_{86}Al_7Ti_7$ HEA have a negligible effect on its fracture behavior.

4. Discussion

4.1. Origin of the anisotropic microstructure

The SLMed $(FeCoNi)_{86}Al_7Ti_7$ HEA has an anisotropic structure with columnar grains along the BD, as presented in section 3.1. According to the solidification theory [47], the grain morphology of SLMed metals depends on local solidification conditions, i.e., the thermal gradient (G) and the solidification rate (R) at the liquid-solid interface of the MP. The derived solidification parameter G/R obtained from the computed transient temperature field determines the microstructural morphology [48]. To analyze the relation between the thermal condition and microstructure of the SLMed HEA, FEM simulation was conducted. Fig. 6a shows the side-view thermal profile in a MP of $(FeCoNi)_{86}Al_7Ti_7$ HEA, from which the variation of G and R as the MP evolves can be obtained, as shown in Fig. 6b. With the liquid front advancing and the MP evolving, G decreases, and R increases rapidly. This transient behavior of G and R with the solidification distance agrees with the results from the literature [49,50]. The present SLMed HEA has a MP depth of 120 μm and a layer thickness of 50 μm, which means that the top area with a thickness of 70 μm will be remelted during the subsequent laser scanning on next layer. In other words, the observed structure in the SLMed HEA corresponds to the bottom area with a thickness of 50 μm. At the bottom of the MP, G is high while R is relatively low, favoring the formation of the columnar grains [51]. Based on the calculated thermal conditions of the MP, the solidification microstructure can be predicted from a reference solidification map of IN718 [52], as shown in Fig. 6c. In the upper right part of the solidification map with high G, columnar grains are conducive to form as the MP begins to

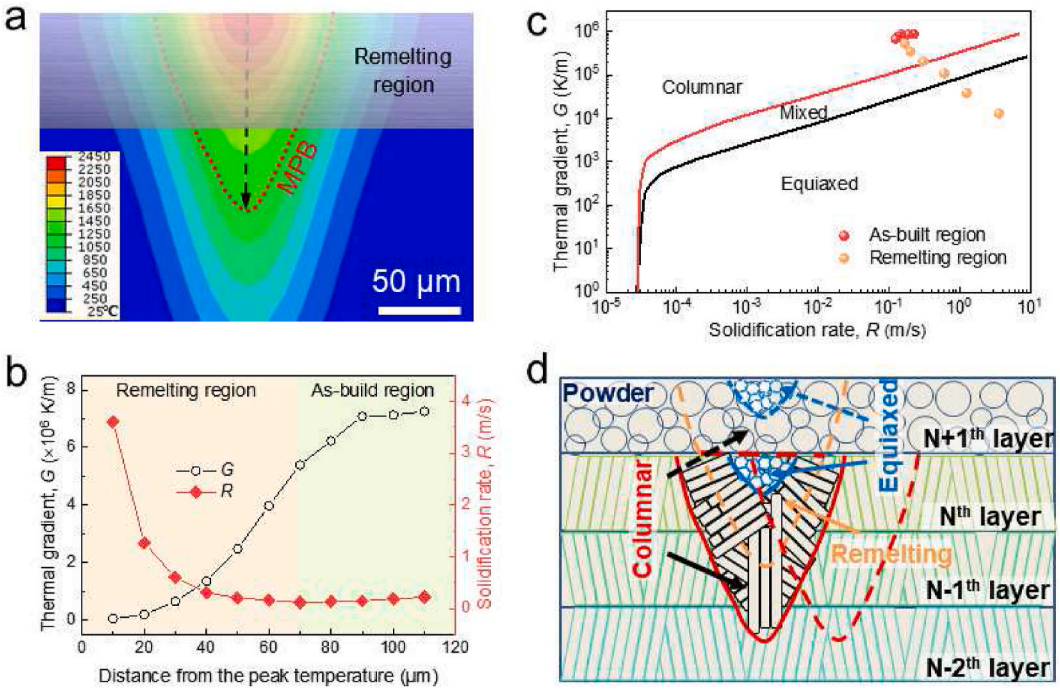

Fig. 6. (a) Side-view thermal profile in a melt pool of $(FeCoNi)_{86}Al_7Ti_7$ HEA. (b) The variations of G (black line) and R (red line) along the liquidus front. (c) Variation of G and R on the reference solidification map. (d) Schematic diagrams showing grain morphology evolution in a melting pool of $(FeCoNi)_{86}Al_7Ti_7$.

solidify (as shown in Fig. 6d). The lower region of the melting pool follows into the columnar-grain region, while the upper region contains equiaxed grains. This microstructural transition aligns with our experimental observations of the melting pool in the top most layer (Fig. S3). The top region will be entirely remelted by the subsequent scanning for depositing the next layer during SLM [50,53], therefore the anisotropic structure with fully columnar grain morphology forms during the SLM process, which displays equiaxed shape from the top view observation.

Another structural characteristic of the present SLMed HEA is the cellular sub-structure with precipitates at cellular boundaries, which is due to the rapid solidification process and element segregation [54], as shown from TEM characterization in Fig. 3. Besides, the cell size (λ) can be calculated using the following equation [54]:

$$\lambda = \alpha(R)^{-\beta} \tag{3}$$

where R is the cooling rate, α is a constant parameter with a value of 183.6, and β is adopted as 1/3 from IN718 superalloy [54]. The calculated cell size is 1.56–3.13 μm, consistent with the experimental value of 1–2 μm in the SLMed HEA. Therefore, it can be concluded that the anisotropic structure with columnar grains and cellular sub-structure arises from the rapid solidification process and adopted scanning strategy during SLM.

4.2. Mechanism of anisotropic yield strength

As revealed in section 3.2, the yield strength of the SLMed $(FeCoNi)_{86}Al_7Ti_7$ HEA varied in samples with different orientations, where 45° sample has a slightly higher yield strength of 752 MPa. For the present SLMed HEA, the yield strength is mainly attributed to grain-boundary strengthening, dislocation strengthening and precipitation strengthening [55,56], which can be expressed as the following equation:

$$\sigma_y = \sigma_0 + kd^{-1/2} + M\alpha Gb\rho^{1/2} + \frac{0.4MGb}{\pi(1-\nu)^{1/2}}\frac{\ln\left(\frac{2\bar{r}}{b}\right)}{L_p} \tag{4}$$

where σ_0 is the lattice friction stress, k is the grain boundary strengthening coefficient, d is the average grain size of classical Hall-Petch relationship, M is the Taylor factor accounting for the crystallographic texture, $\alpha = 0.2$ is a constant for FCC alloys [55], $G = 77$ GPa is the shear modulus of the SLMed HEA [56], b is the Burgers vector adopted 0.255 nm [55], and ρ is the dislocation density. $\nu = 0.3$ is the Poisson ratio; $\bar{r} = \sqrt{2/3}\cdot r$ is the mean particle radius on the slip planes, where $r = \sim 100$ nm; $L_p = 2\bar{r}\left(\sqrt{\frac{\pi}{4f}} - 1\right)$ is the mean interparticle spacing, and f is the volume fraction of the precipitates. The second, third, and fourth terms in Eq. (4) correspond to the grain-boundary strengthening (σ_{GB}), dislocation strengthening (σ_ρ), and precipitation strengthening (σ_{L21}), respectively.

Given the chemical composition of the present HEA is almost identical to the CoCrNi-based medium-entropy alloy [57], the values of σ_0 and k are adopted as 216 MPa and 568 MPa $\mu m^{1/2}$. The average grain sizes of the 0°, 45°, and 90° samples are 12.6 μm, 13.0 μm and 17.1 μm according to EBSD calculation, respectively, as shown in Fig. 7a–c. Thus, the GB strengthening contribution for 0°, 45°, and 90° samples are estimated to be ~376 MPa, ~374 MPa, and ~353 MPa, respectively.

The SLMed HEA possesses a pronounced <0 0 1> crystallographic texture along BD, which leads to a variance in the Taylor factor among the three samples and influences the yield strength. Fig. 7d–f shows the Talyor factor maps of three samples, from which the average M values were calculated to be 3.12, 3.20, and 2.93 for 0°, 45°, and 90° samples, respectively. The dislocation density (ρ) for SLMed HEA is 5.4×10^{14} m^{-2}, which was estimated from the XRD measurement [55,58]. Accordingly, the estimated contribution of dislocation hardening in 0°, 45°, and 90° samples are ~285 MPa, ~292 MPa, and ~267 MPa, respectively. Obviously, the dislocation strengthening is distinguished in different samples, contributing to the anisotropy in yield strength.

Precipitation strengthening originates from $L2_1$ nano-precipitates through the Orowan bowing mechanisms [56], as expressed by the last term in Eq. (4). In the present SLMed HEA, r is ~100 nm, and f is ~2.3 %. Therefore, the precipitation strengthening contribution for 0°, 45°, and 90° samples are ~76 MPa, ~78 MPa, and ~72 MPa,

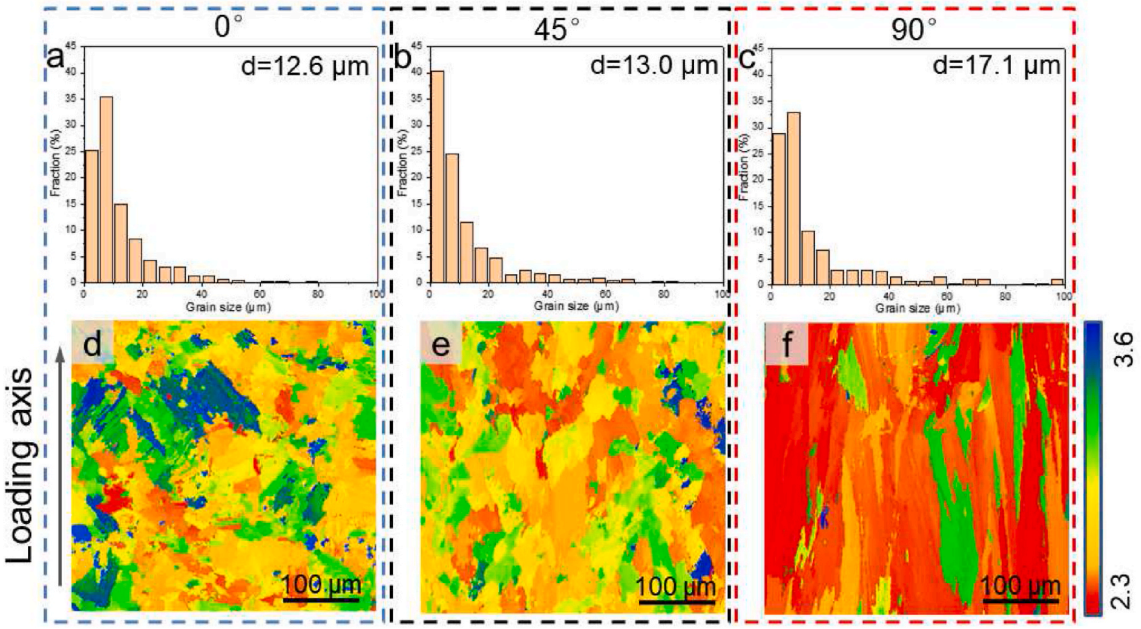

Fig. 7. The grain size distribution and Taylor factor maps of the SLMed HEA samples with respect to different loading directions: (a, d) 0°, (b, e) 45° and (c, f) 90°.

respectively, which has little effect on the anisotropy in yield strength.

Fig. 8 summarizes the strength contributions from the aforementioned strengthening mechanisms in 0°, 45°, and 90° samples. The calculated yield strengths of 0°, 45°, and 90° samples are ~737 MPa, ~744 MPa, and ~692 MPa, respectively, consistent with the experimental results. 45° sample has the highest yield stress, which also matches well with the experimental observation and observations in other materials produced by 3D printing [59]. Therefore, it can be concluded that the difference in grain morphology and texture, i.e., average grain size and Taylor factor, leads to anisotropy in the yield strength of the present SLMed HEA.

4.3. Mechanism of anisotropic tensile elongation

The present SLMed $(FeCoNi)_{86}Al_7Ti_7$ HEA exhibits slight strength anisotropy but distinct ductility anisotropy, which would affect its service performance as structural materials. To explore the origin of anisotropy in tensile elongation, the interrupted tensile tests were performed for observing crack propagation behavior. Given there is no

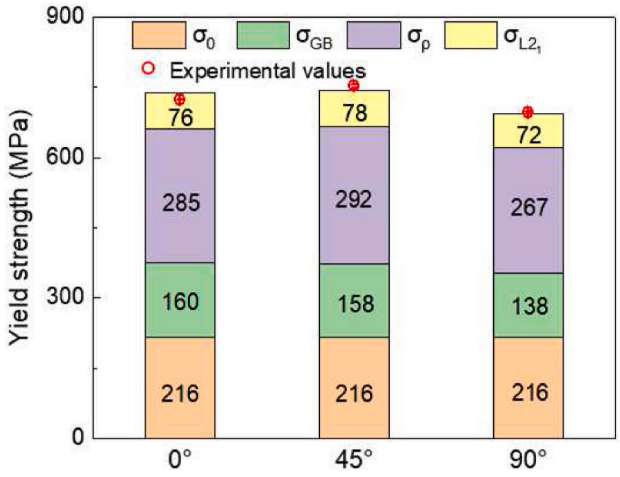

Fig. 8. Strengthening contributions from different microstructural factors of the SLMed HEA under different loading directions.

significant difference in tensile ductility between 45° and 90° samples, and the tensile testing were interrupted at the strain approaching to necking. i.e., 13.2 % and 11.2 % for 45° and 90° samples, respectively, as shown in Fig. 4, the following section will focus on the 0° and 90° samples.

Fig. 9 shows the EBSD-IPF and KAM images of 0° and 90° samples with tensile strain of ~25 % and ~10 %, respectively. Fig. 9a shows a blunt crack with a length of ~64 μm in the deformed 0° sample, where crack propagation occurs through both inter and transgranular modes [27]. The crack is deflected more or less when propagated along the grain boundary, resulting in greater resistance to crack propagation and a more tortuous crack propagation path. In contrast, 90° sample exhibits a large and relatively straight crack. Crack propagates essentially along the continuous MPBs, as presented in Fig. 9c, providing a more favorable and direct crack pathway through the sample.

KAM is usually employed to evaluate the local plastic strain in materials, from which the residual strain distribution can be obtained. Fig. 9b and d shows KAM images of 0° and 90° samples after tensile deformation (25 % and 10 % strain, respectively), where blue and red represent the minimum and maximum residual strain, respectively. 0° sample exhibits severe plastic deformation throughout the whole region (Fig. 9b). Focusing on the strain distribution near the crack, a much lower strain (the blue region) is situated along the crack, possibly due to the stress relief during crack propagation. Particularly, there is a large region with considerable strain concentration on the crack tips (red and green regions), suggesting that the grain boundaries have a strong hindering effect on crack propagation. Meanwhile, the crack is likely to branch along grain boundaries with deflection (as indicated by the white arrows), indicative of intergranular mode between grains with different orientations. In contrast, the strain is substantially lower in the 90° sample because of experiencing lower plastic strain. Similarly, the higher residual strain can be observed at the cellular boundaries, indicating a potential site for crack initiation.

Crack propagation behavior in the 0° and 90° samples was further analyzed by SEM and schematically illustrated, as shown in Fig. 10. The crack propagation path in the 0° sample with 25 % strain appears rough and zig-zagged, indicating that the crack propagation is accompanied by the substantial plastic deformation, as shown in Fig. 10a. The crack propagates via an intergranular-transgranular-intergranular mode through grains and cells. Here, intergranular path propagates along the

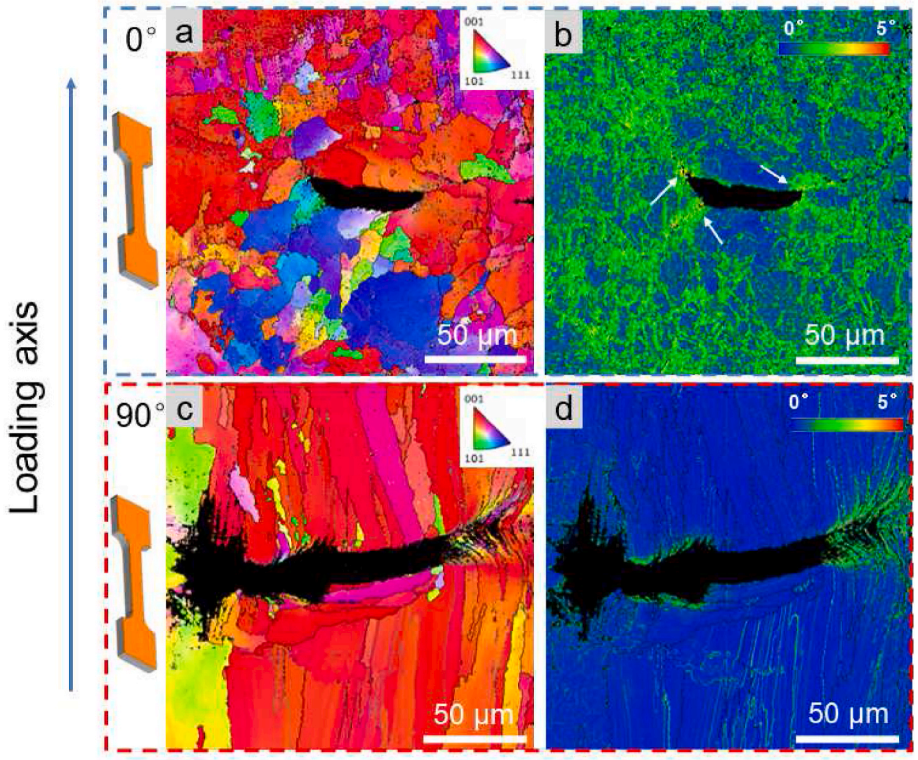

Fig. 9. EBSD-IPF along loading axis and KAM images of crack propagation path in (a, b) 0° sample with 25 % strain and (c, d) 90° sample with 10 % strain.

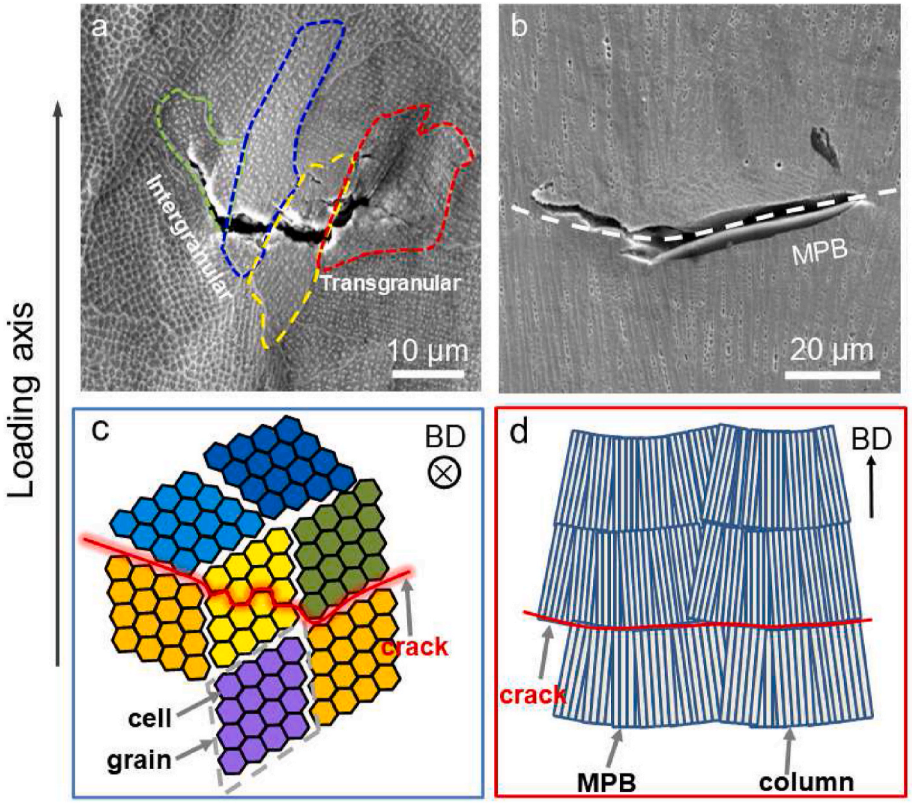

Fig. 10. SEM images and the corresponding schematic diagrams showing crack propagation path in (a, c) 0° sample and (b, d) 90° sample.

grain boundaries, and transgranular propagation is more likely to occur along the cellular boundaries. The HAGBs play a positive role in the crack deflection along the grain boundaries, leading to the more tortuous crack propagation path and higher ductility in the 0° sample (Fig. 10c).

In contrast, 90° sample with 10 % strain displays a completely

different crack propagation path, where the crack follows a straight line along the MPBs, as shown in Fig. 10b. It was reported that MPBs are weak points due to the higher intrinsic defects and larger thermal stress concentration [29,46], making the crack propagation energetically more favorable along the MPB than across the MP. In the 90° sample, a large fraction of flat MPBs is oriented perpendicular to the loading force, which provides an easy path for crack propagation through MPB decohesion [44,46], thereby showing less resistance for crack propagation and premature failure during the plastic deformation (Fig. 10d). The MPB decohesion behavior in the 90° sample can be further confirmed by optical micrograph, as shown in Fig. S4.

5. Conclusions

In conclusion, $(FeCoNi)_{86}Al_7Ti_7$ HEA, manufactured through SLM, exhibits exceptional formability and mechanical properties. Both experimental and theoretical approaches were employed to explore the structural and mechanical anisotropy of the printed HEA. The following conclusions can be obtained.

(1) The SLMed HEA exhibits an anisotropic structure parallel and perpendicular to the BD composed of MPs with semi-elliptical and strike-like shape, <0 0 1> textured grains with columnar and equiaxial shape, as well as the columnar and cellular substructure with $L2_1$-phase nanoprecipitates along cell walls, induced by the rapid solidification and supercooling process.
(2) Tensile testing reveals that the SLMed HEA exhibits slight anisotropy in strength but significant anisotropy in ductility. The 45° sample has the highest yield strength of 752 MPa, which is 4 % and 8 % higher than that in 0° and 90° samples, respectively. However, 0° sample has a tensile elongation of 31.5 %, approximately 2.6 times higher than that of 45° and 90° samples.
(3) The anisotropy in strength arises from variations in grain size and crystallographic texture across different orientations. Specifically, the 45° sample, characterized by a smaller grain size and a higher Taylor factor, demonstrates a higher yield strength.
(4) The crack propagation behavior differences originating from anisotropic microstructure in 0°, 45° and 90° directions finally induce the anisotropic tensile elongation. For the 90° sample, a large fraction of flat MPBs perpendicular to the loading force provides an easy path for crack propagation through MPB decohesion, leading to moderate plasticity. In contrast, the crack in the 0° sample propagates along the cellular boundaries by intergranular and transgranular mode, resulting in a more tortuous crack propagation path and higher ductility.

Data availability

Experimental data from this study are available from Prof. Lin Liu from Huazhong University of Science and Technology upon reasonable request.

CRediT authorship contribution statement

Li-Xue Liu: Investigation, methodology, experiments, writing – original draft. **Jie Pan:** Formal analysis, visualization, writing – review & editing, funding acquisition. **Peng-Cheng Zhang:** Formal analysis, simulation. **Cheng Zhang:** Formal analysis, visualization. **Jing-Yu Xu:** Formal analysis. **Rong Guo:** Formal analysis. **Zi-Bin Chen:** Formal analysis, simulation. **K.C. Chan**: Formal analysis, simulation. **Lin Liu:** Resources, supervision, writing – review & editing, funding acquisition.

Declaration of competing interest

The authors declare that they have no known competing financial interests or personal relationships that could have appeared to influence the work reported in this paper.

Acknowledgement

This work is supported by the National Natural Science Foundation of China (Nos. 52061160483, 52022100 and 52371155). J. P. also acknowledge the financial support from Key R&D Program of Hubei (2022BAA023). The authors are also grateful to the Analytical and Testing Center, Huazhong University of Science and Technology for technical assistance. Z.B.C would also acknowledge support from The Hong Kong Polytechnic University (P0043015 and P0041361).

Appendix A. Supplementary data

Supplementary data to this article can be found online at https://doi.org/10.1016/j.jmrt.2023.10.161.

References

[1] Cantor B, Chang ITH, Knight P, Vincent AJB. Microstructural development in equiatomic multicomponent alloys. Mater Sci Eng, A 2004;375:213–8.
[2] Yeh JW, Chen SK, Lin SJ, Gan JY, Chin TS, Shun TT, et al. Nanostructured high-entropy alloys with multiple principal elements: novel alloy design concepts and outcomes. Adv Eng Mater 2004;6:299–303.
[3] Shi Y, Yang B, Xie X, Brechtl J, Dahmen KA, Liaw PK. Corrosion of Al_xCoCrFeNi high-entropy alloys: Al-content and potential scan-rate dependent pitting behavior. Corrosion Sci 2017;119:33–45.
[4] Wang S, Wu M, Shu D, Zhu G, Wang D, Sun B. Mechanical instability and tensile properties of TiZrHfNbTa high entropy alloy at cryogenic temperatures. Acta Mater 2020;201:517–27.
[5] Ma Q, Yang H, Wang Z, Shi X, Liaw PK, Qiao J. High strength and ductility in partially recrystallized $Fe_{40}Mn_{20}Cr_{20}Ni_{20}$ high-entropy alloys at cryogenic temperature. Microstructures 2022;2:2022015.
[6] George EP, Curtin WA, Tasan CC. High entropy alloys: a focused review of mechanical properties and deformation mechanisms. Acta Mater 2020;188:435–74.
[7] Xu D, Wang M, Li T, Wei X, Lu Y. A critical review of the mechanical properties of CoCrNi-based medium-entropy alloys. Microstructures 2022;2:2022001.
[8] Yan X, Zou Y, Zhang Y. Properties and processing technologies of high-entropy alloys. Mater Futures 2022;1:022002.
[9] Li J, Yang H, Wang WY, Kou H, Wang J. Thermal–mechanical processing and strengthen in Al_xCoCrFeNi high-entropy alloys. Front Mater 2021;7:585602.
[10] Zhang W, Chabok A, Kooi BJ, Pei Y. Additive manufactured high entropy alloys: a review of the microstructure and properties. Mater Des 2022;220:110875.
[11] Wang M, Lu Y, Wang T, Zhang C, Cao Z, Li T, et al. A novel bulk eutectic high-entropy alloy with outstanding as-cast specific yield strengths at elevated temperatures. Scripta Mater 2021;204:114132.
[12] Wu H, Xie J, Yang H, Shu D, Hou G, Li J, et al. A cost-effective eutectic high entropy alloy with an excellent strength–ductility combination designed by VEC criterion. J Mater Res Technol 2022;19:1759–65.
[13] Alaneme KK, Anaele JU, Kareem SA. Hot deformability, microstructural evolution and processing map assessment of high entropy alloys: a systematic review. J Mater Res Technol 2023;26:1754–84.
[14] Guan S, Wan D, Solberg K, Berto F, Welo T, Yue TM, et al. Additively manufactured CrMnFeCoNi/AlCoCrFeNi$Ti_{0.5}$ laminated high-entropy alloy with enhanced strength-plasticity synergy. Scripta Mater 2020;183:133–8.
[15] Dong B, Wang Z, Zhu H, Muránsky O, Qiu Z, Shen C, et al. Low neutron cross-section FeCrVTiNi based high-entropy alloys: design, additive manufacturing and characterization. Microstructures 2022;2:2022003.
[16] Peng X, Cao X, Wang Y, Dong Y, Li Z, Xu H, et al. Design, microstructure, and mechanical property of negative Poisson's ratio porous structure fabricated by LPBF of AlCoCrFeNi$_{2.1}$ eutectic high-entropy-alloy. J Mater Res Technol 2023;24:2028–40.
[17] Zhu ZG, Nguyen QB, Ng FL, An XH, Liao XZ, Liaw PK, et al. Hierarchical microstructure and strengthening mechanisms of a CoCrFeNiMn high entropy alloy additively manufactured by selective laser melting. Scripta Mater 2018;154:20–4.
[18] Kuzminova YO, Firsov DG, Dagesyan SA, Konev SD, Sergeev SN, Zhilyaev AP, et al. Fatigue behavior of additive manufactured CrFeCoNi medium-entropy alloy. J Alloys Compd 2021;863:158609.
[19] Sun Z, Tan X, Wang C, Descoins M, Mangelinck D, Tor SB, et al. Reducing hot tearing by grain boundary segregation engineering in additive manufacturing: example of an Al_xCoCrFeNi high-entropy alloy. Acta Mater 2021;204:116505.
[20] Fu Z, Zhang Y, Li Z, Lu Y, Wu X, Wang H. Hierarchically heterogeneous microstructure enables ultrahigh-strength and good ductility in selective laser melted eutectic high-entropy alloys. J Mater Res Technol 2023;24:3300–8.
[21] Kim Y, Kim M, Lee K. 1.45 GPa ultrastrong cryogenic strength with superior impact toughness in the in-situ nano oxide reinforced CrMnFeCoNi high-entropy alloy matrix nanocomposite manufactured by laser powder bed fusion. J Mater Sci Technol 2022;97:10–9.

[22] Bertsch KM, Meric de Bellefon G, Kuehl B, Thoma DJ. Origin of dislocation structures in an additively manufactured austenitic stainless steel 316L. Acta Mater 2020;199:19–33.
[23] Kok Y, Tan XP, Wang P, Nai MLS, Loh NH, Liu E, et al. Anisotropy and heterogeneity of microstructure and mechanical properties in metal additive manufacturing: a critical review. Mater Des 2018;139:565–86.
[24] Park JM, Choe J, Park HK, Son S, Jung J, Kim T-S, et al. Synergetic strengthening of additively manufactured $(CoCrFeMnNi)_{99}C_1$ high-entropy alloy by heterogeneous anisotropic microstructure. Addit Manuf 2020;35:101333.
[25] Shifeng W, Shuai L, Qingsong W, Yan C, Sheng Z, Yusheng S. Effect of molten pool boundaries on the mechanical properties of selective laser melting parts. J Mater Process Technol 2014;214:2660–7.
[26] Clare AT, Mishra RS, Merklein M, Tan H, Todd I, Chechik L, et al. Alloy design and adaptation for additive manufacture. J Mater Process Technol 2022;299:117358.
[27] Paul MJ, Liu Q, Best JP, Li X, Kruzic JJ, Ramamurty U, et al. Fracture resistance of AlSi10Mg fabricated by laser powder bed fusion. Acta Mater 2021;211:116869.
[28] Kuo Y, Horikawa S, Kakehi K. The effect of interdendritic δ phase on the mechanical properties of Alloy 718 built up by additive manufacturing. Mater Des 2017;116:411–8.
[29] Jeon JM, Park JM, Yu J-H, Kim JG, Seong Y, Park SH, et al. Effects of microstructure and internal defects on mechanical anisotropy and asymmetry of selective laser-melted 316L austenitic stainless steel. Mater Sci Eng, A 2019;763:138152.
[30] Xiang S, Li J, Luan H, Amar A, Lu S, Li K, et al. Effects of process parameters on microstructures and tensile properties of laser melting deposited CrMnFeCoNi high entropy alloys. Mater Sci Eng, A 2019;743:412–7.
[31] Wu Z, He M, Cao H, Wang S, Chen R, Cao B, et al. Ultrahigh-strength and ductile CoCrFeNi-based high-entropy alloys manufactured by laser powder bed fusion with multiple strengthening mechanisms. J Mater Res Technol 2023;25:2948–60.
[32] Zhang C, Feng K, Kokawa H, Li Z. Correlation between microstructural heterogeneity and anisotropy of mechanical properties of laser powder bed fused CoCrFeMnNi high entropy alloy. Mater Sci Eng, A 2022;855:143920.
[33] Zhang W, Wang H, Kooi BJ, Pei Y. Additive manufacturing of interstitial-strengthened high entropy alloy: scanning strategy dependent anisotropic mechanical properties. Mater Sci Eng, A 2023;872:144978.
[34] Yang T, Zhao YL, Tong Y, Jiao ZB, Wei J, Cai JX, et al. Multicomponent intermetallic nanoparticles and superb mechanical behaviors of complex alloys. Science 2018;362:933–7.
[35] Liu L, Pan J, Zhang C, Xu J, Guo R, Liu L. Achieving high strength and ductility in a 3D-printed high entropy alloy by cooperative planar slipping and stacking fault. Mater Sci Eng, A 2022;843:143106.
[36] Williamson WHHGK. X-ray line broadening from filed aluminium and wolfram. Acta Metall 1953;1:22–31.
[37] Williamson GK, Smallman III RE. Dislocation densities in some annealed and cold-worked metals from measurements on the X-ray debye-scherrer spectrum. Philos Mag 1956;1:34–46.
[38] Andreau O, Koutiri I, Peyre P, Penot J, Saintier N, Pessard E, et al. Texture control of 316L parts by modulation of the melt pool morphology in selective laser melting. J Mater Process Technol 2019;264:21–31.
[39] Santos Macías JG, Douillard T, Zhao L, Maire E, Pyka G, Simar A. Influence on microstructure, strength and ductility of build platform temperature during laser powder bed fusion of AlSi10Mg. Acta Mater 2020;201:231–43.
[40] Ni M, Chen C, Wang X, Wang P, Li R, Zhang X, et al. Anisotropic tensile behavior of in situ precipitation strengthened Inconel 718 fabricated by additive manufacturing. Mater Sci Eng, A 2017;701:344–51.
[41] Seol JB, Bae JW, Kim JG, Sung H, Li Z, Lee HH, et al. Short-range order strengthening in boron-doped high-entropy alloys for cryogenic applications. Acta Mater 2020;194:366–77.
[42] Wu Y, Zhang F, Yuan X, Huang H, Wen X, Wang Y, et al. Short-range ordering and its effects on mechanical properties of high-entropy alloys. J Mater Sci Technol 2021;62:214–20.
[43] Liang X, Kang L, Li H, Wang R, Wu Q, Liu B, et al. Effect of annealing temperature on anisotropy of mechanical properties in powder metallurgy $FeCoCrNiN_{0.07}$ high-entropy alloy sheets. Mater Sci Eng, A 2021;823:141585.
[44] Maconachie T, Leary M, Zhang J, Medvedev A, Sarker A, Ruan D, et al. Effect of build orientation on the quasi-static and dynamic response of SLM AlSi10Mg. Mater Sci Eng, A 2020;788:139445.
[45] Guo R, Pan J, Liu L. Achieving dual-phase structure and improved mechanical properties in $AlCoCrFeTi_{0.5}$ high-entropy alloys by addition of Ni. Mater Sci Eng, A 2022;831:142194.
[46] Ben DD, Ma YR, Yang HJ, Meng LX, Shao XH, Liu HQ, et al. Heterogeneous microstructure and voids dependence of tensile deformation in a selective laser melted AlSi10Mg alloy. Mater Sci Eng, A 2020;798:140109.
[47] Kobryn PA, Semiatin SL. Microstructure and texture evolution during solidification processing of Ti–6Al–4V. J Mater Process Technol 2003;135:330–9.
[48] Knapp GL, Raghavan N, Plotkowski A, DebRoy T. Experiments and simulations on solidification microstructure for Inconel 718 in powder bed fusion electron beam additive manufacturing. Addit Manuf 2019;25:511–21.
[49] Li H, Huang Y, Sun J, Lu Y. The relationship between thermo-mechanical history, microstructure and mechanical properties in additively manufactured CoCrFeMnNi high entropy alloy. J Mater Sci Technol 2021;77:187–95.
[50] Raghavan N, Simunovic S, Dehoff R, Plotkowski A, Turner J, Kirka M, et al. Localized melt-scan strategy for site specific control of grain size and primary dendrite arm spacing in electron beam additive manufacturing. Acta Mater 2017;140:375–87.
[51] Bermingham M, StJohn D, Easton M, Yuan L, Dargusch M. Revealing the mechanisms of grain nucleation and formation during additive manufacturing. J Occup Med 2020;72:1065–73.
[52] Sames WJ, Unocic KA, Dehoff RR, Lolla T, Babu SS. Thermal effects on microstructural heterogeneity of Inconel 718 materials fabricated by electron beam melting. J Mater Res 2014;29:1920–30.
[53] DebRoy T, Wei HL, Zuback JS, Mukherjee T, Elmer JW, Milewski JO, et al. Additive manufacturing of metallic components – process, structure and properties. Prog Mater Sci 2018;92:112–224.
[54] Wang W, Zhu C, Zeng J, Lu C, Qian H, Xu H, et al. Microstructures and Nb-rich precipitation behaviors of inconel 718 superalloy under sub-rapid solidification process. Metall Mater Trans A 2020;51:2306–17.
[55] He JY, Wang H, Huang HL, Xu XD, Chen MW, Wu Y, et al. A precipitation-hardened high-entropy alloy with outstanding tensile properties. Acta Mater 2016;102:187–96.
[56] Wu Y, Zhao X, Chen Q, Yang C, Jiang M, Liu C, et al. Strengthening and fracture mechanisms of a precipitation hardening high-entropy alloy fabricated by selective laser melting. Virtual Phys Prototyp 2022;17:451–67.
[57] Zhao YL, Yang T, Tong Y, Wang J, Luan JH, Jiao ZB, et al. Heterogeneous precipitation behavior and stacking-fault-mediated deformation in a CoCrNi-based medium-entropy alloy. Acta Mater 2017;138:72–82.
[58] Zhao YH, Liao XZ, Jin Z, Valiev RZ, Zhu YT. Microstructures and mechanical properties of ultrafine grained 7075 Al alloy processed by ECAP and their evolutions during annealing. Acta Mater 2004;52:4589–99.
[59] Sun S, Koizumi Y, Kurosu S, Li Y, Matsumoto H, Chiba A. Build direction dependence of microstructure and high-temperature tensile property of Co–Cr–Mo alloy fabricated by electron beam melting. Acta Mater 2014;64:154–68.